A NOVEL EXPERIMENTAL APPROACH TO THE AERODYNAMIC TESTING OF WIND ASSISTED SHIP AND YACHT SAILS

Jean-Baptiste R. G. Souppez, University of Edinburgh, jean-baptiste.souppez@ed.ac.uk

ABSTRACT

Highly cambered profiles yield powerful wind-assisted ship wings and yacht sails. However, their complex aerodynamics governed by flow separation remains to be fully understood. Particle image velocimetry in water tunnels may lead to new breakthroughs, but limitations exist due to the necessary high spatial and temporal resolution. Force measurements and flow visualisation were undertaken on circular arcs and sails to ascertain the viability of this novel experimental approach. The results reveal that (i) a linear blockage correction can be devised; (ii) a blockage-independent critical Reynolds number and critical angle of attack exist; and (iii) a force crisis occurs because of the suppressed relaminarisation of the boundary layer downstream of the leading-edge separation bubble. Ultimately, water tunnel testing is demonstrated to be a pertinent experimental methodology. These findings provide novel insights into the experimental testing of wind-assisted ship and yacht sails, and may contribute to improving their performance by design.

KEYWORDS

Keywords: Fluid Dynamics, PIV, Flow Visualisation, Yacht Sails, Wind Assisted Ship Propulsion.

1. INTRODUCTION

Wind-assisted ship wings, such as DynaRigs, and downwind yacht sails are thin wings with a sharp leading edge. They are further characterised by a high camber-to-chord ratio. For incidences above the ideal angle of attack (where the stagnation point lies at the leading edge) and below stall, flow separation occurs on the suction (leeward) side. This leads to the formation of a leading-edge separation bubble (LESB). Flow reattachment occurs downstream of the LESB and upstream of the large region of trailing-edge separation. Indeed, while a high camber is desirable to generate high lift, the aerodynamics is governed by flow separation, which remains to be fully understood.

While extensive force measurements have been undertaken in wind tunnels for both wind-assisted ships (He et al., 2015; Bordogna et al., 2018; Bordogna, 2020; Bordogna et al., 2020; Zhang et al., 2021; Kume et al., 2022) and yacht sails (Fossati et al., 2006; Viola and Flay, 2009; Viola et al., 2013; Bot et al., 2014; Campbell, 2014), quantitative flow visualisation using particle image velocimetry (PIV) is lacking (Gauvin and Banks, 2020; Giovannetti et al., 2022). PIV is a non-intrusive optical method where the motion of a fluid is visualised by illuminating seeding particles with a thin laser sheet (Raffel et al. 2018). However, there are experimental difficulties associated with undertaking PIV in wind tunnels. Because the smoke particles employed to seed the air do not reflect light well, particle illumination issues arise, requiring more powerful and, thus, more expensive lasers. Such powerful lasers cause light reflection on the geometry under study, which affects the flow visualisation. Furthermore, as smoke dissipates, particle density in the flow is inconsistent and impossible to reproduce, leading to high uncertainty.

In contrast, undertaking PIV in water enables the use of highly reflective silver-coated hollow glass spheres, leading to lower power and more affordable lasers, and alleviating reflection issues. Additionally, particle density can be maintained and reproduced, leading to comparatively lower uncertainty than in air. Consequently, undertaking PIV in water tunnels could be a promising experimental methodology that may yield new breakthroughs in aerodynamics, but it requires a high spatial and temporal resolution, only achieved by increasing the model size and decreasing the stream velocity, respectively.

Firstly, large model sizes are needed to ensure high-resolution flow visualisation. The consequence is a large blockage ratio, defined as the ratio of the frontal area of the geometry to the tunnel's cross-sectional area, causing an increase in the flow speed around the geometry compared to the free-stream velocity and an artificial increase in force coefficients. Lasher et al. (2005) recommended a blockage ratio below 0.050 for sails. However, recent PIV measurements have been conducted at much higher blockage ratios (Arredondo-Galeana and Viola, 2018; Molina et al., 2019; Bot, 2020; Arredondo-Galeana et al., 2023). Highly cambered plates and wings are beyond the scope of established blockage corrections (Pope and Harper,1966; ESDU, 1995; ESDU, 1998; Barlow et al., 1999). Thus, whether a suitable blockage correction can be established warrants further research.

Secondly, a low stream velocity is needed to maximise the temporal resolution, resulting in low Reynolds numbers. Water tunnel tests are undertaken at chord-based Reynolds numbers of the order of 10^4 (Arredondo-Galeana & Viola, 2018; Arredondo-Galeana et al., 2023). This is in contrast to wind tunnel tests being conducted at 10^5 (Viola and Flay, 2009; Bot et al., 2014), and full-scale sails operating at 10^6-10^7 (Collie, 2006; Viola & Flay, 2010; Deparday et al., 2018). As such, the minimum Reynolds number for experimental testing to yield accurate full-scale results is to be ascertained.

The aim of this paper is to investigate the relevance of undertaking force measurement and PIV in water tunnels to obtain force coefficients and quantitative flow fields for wind-assisted ship and yacht sail aerodynamics. Specifically, whether the limitations associated with the high blockage ratios and low Reynolds numbers can be overcome will be tackled. This will be applied to two cases: a two-dimensional circular arc representative of rigid wings such as DynaRigs, and a three-dimensional sail.

The remainder of this paper is structured as follows. Section 2 introduces the two geometries and experimental facilities employed in this study, as well as the methodology inherent to force measurement and flow visualisation and their associated uncertainty. Then, Section 3 presents a validation of the proposed methodology and results for the effect of blockage, low Reynolds number, and flow visualisation. Finally, Section 4 summarises the main findings and their wider impact.

2. METHODOLOGY

2.1 TOWING TANK TESTING

Circular arcs are representative of the section employed for wind-assisted propulsion solutions (Khan et al., 2021, Souppez and Viola, 2021) such as DynaRigs (Bordogna et al., 2018; Zeng et al., 2023), crescent sails (Atkinson and Binns, 2018; Zhu et al., 2022) and downwind yacht sails (Collie, 2006; Souppez et al. 2019; Bot, 2020). The geometry employed in this work, depicted in Figure 1, features a camber-to-chord ratio $y_c/c = 0.2232$, identical to that of Velychko (2014), Bot et al. (2016) and Bot (2020).

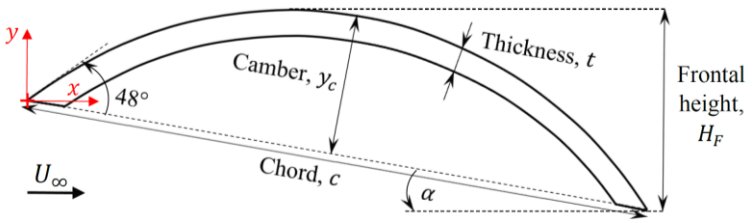

Figure 1: 2D circular arc geometry.

To cover a wide range of Reynolds numbers ($53\,530 \leq Re \leq 218\,000$), three carbon fibre circular arcs were manufactured, namely a small (chord $c = 100$ mm), medium ($c = 150$ mm) and large ($c = 150$ mm) arc. The geometrical characteristics are presented in Table 1.

Table 1: Geometric dimensions of the three circular arcs employed.

Circular Arc	**Small**	**Medium**	**Large**
Chord, c [mm]	100	150	200
Span, s [mm]	370	370	370
Aspect ratio, $AR = s^2/A$ [-]	3.70	2.47	1.85
Camber, y_c [mm]	22.32	33.48	44.64
Camber-to-chord ratio y_c/c [-]	0.2232	0.2232	0.2232
Thickness, t [mm]	1.80	1.80	1.80
Thickness-to-chord ratio t/c [-]	0.0180	0.0120	0.0090
Radius of curvature, r [mm]	67.16	100.75	134.33

For the range of angles of attack α investigated, namely $0° \leq \alpha \leq 25°$, the frontal height H_F is computed as

$$H_F = r - (r - y_c)\cos\alpha + 0.5c\sin\alpha \tag{1}$$

Force measurements were undertaken in the towing tank at Solent University, having a length of 60 m, width of 3.7 m, depth of 1.85 m deep, and maximum carriage speed of 4.6 m s^{-1} (Dewavrin and Souppez, 2018). Experiments were conducted for specific values of the chord-based Reynolds number Re, defined as

$$Re = \frac{\rho U_\infty c}{\mu}, \tag{2}$$

where ρ is the water density, U_∞ is the freestream flow velocity, and μ is the dynamic viscosity. The small arc was tested at $Re = 53\,530$, as in Velychko (2014), and $Re = 68\,200$, as in Bot et al. (2016). The medium arc was tested at $Re = 150\,000$ to provide intermediate data. The large arc was tested at $Re = 218\,000$, as in Bot et al. (2016). The three arc sizes were necessary to operate at a high enough speed to minimize noise in the data without experiencing vibration at higher speeds.

In the towing tank, tests can be undertaken without the blockage effects associated with a high blockage ratio A_F/A_S, where A_F is the projected frontal area of the model, and A_S is the cross-sectional area. For the two-dimensional (2D) case under consideration, $A_F/A_S \equiv H_F/d$, where d is the distance between the side walls of the towing tank. To investigate the effect of blockage on the forces, adjustable side walls were employed. Each arc was fitted between end plates to achieve an infinite aspect ratio. The spanwise axis is vertically centred in the middle of the towing tank side walls so that $d = 3700$ mm. Adjustable side walls 1200 mm ($6c$) long by 600 mm ($3c$) deep are employed to increase the blockage ratio, with $d = 1180$ mm, 550 mm and 340 mm, as shown in Figure 2.

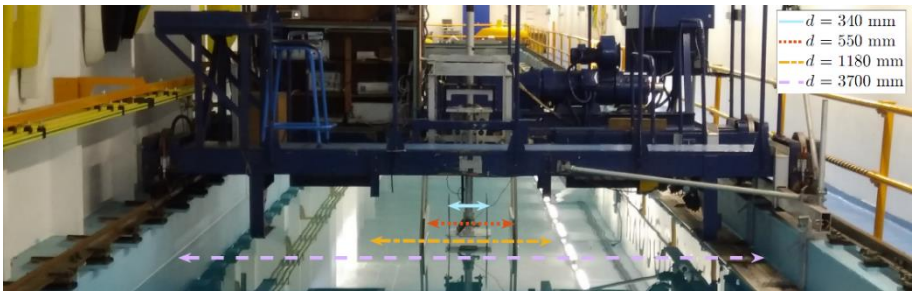

Figure 2: Towing tank setup for $d = 550$ mm.

2.2 WATER TUNNEL TESTING

Further experiments were conducted in the water tunnel at the University of Edinburgh. The water tunnel is 8 m long, 0.40 m wide, and 0.90 m deep with a flat horizontal bed (Arredondo-Galeana, 2019). The static water level was 0.34 m. The water tunnel was employed for force measurement and PIV of the large circular arc and the three-dimensional (3D) yacht sail, as designed by Braun et al. (2016). To investigate blockage effects, three sails were 3D printed, namely a small (average chord $\bar{c} = 85.94$ mm), medium ($\bar{c} = 107.42$ mm) and large ($\bar{c} = 128.90$ mm) sail. The geometrical characteristics are introduced in Table 2, and a cross-section at mid-span is depicted in Figure 3.

Table 1: Geometric dimensions of the three circular arcs employed.

Sail	Small	Medium	Large
Average chord, $\bar{c}$ [mm]	85.94	107.42	128.90
Span, s [mm]	130	162.5	195
Surface area, A [mm^2]	11 172	17 456	25 136
Aspect ratio, AR [-]	1.513	1.513	1.513
Thickness, t [mm]	2.00	2.50	3.00
Thickness-to-chord ratio t/c [-]	0.0233	0.0233	0.0233

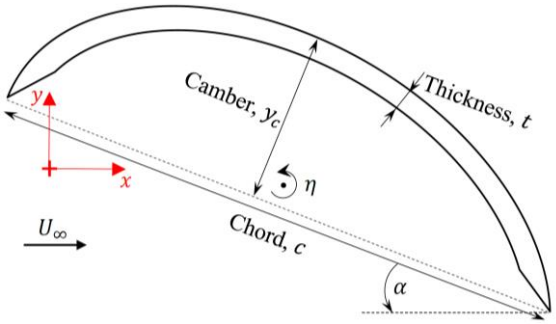

Figure 3: Mid-span section through the 3D sail geometry of Braun et al. (2016).

Experiments were conducted at chord-based Reynolds number $5\,870 \leq Re_{\bar{c}} \leq 61\,870$, with a main focus at $Re_{\bar{c}} = 32\,210$, where $Re_{\bar{c}}$ is defined as

$$Re_{\bar{c}} = \frac{\rho U_\infty \bar{c}}{\mu}. \tag{3}$$

The experimental setups are shown in Figure 4(a) and 4(b) for the circular arc and spinnaker, respectively. Because of its two-dimensionality, a single PIV plane is captured for the circular arc. However, for the three-dimensional sail, 5 planes are investigated, namely $z/s = 0.05$, 0.37, 0.57, 0.70 and 0.88, as depicted in Figure 5. Here, z/s represents the spanwise position, with $z/s = 0$ being the bottom of the sail, and $z/s = 1$ being the top of the sail.

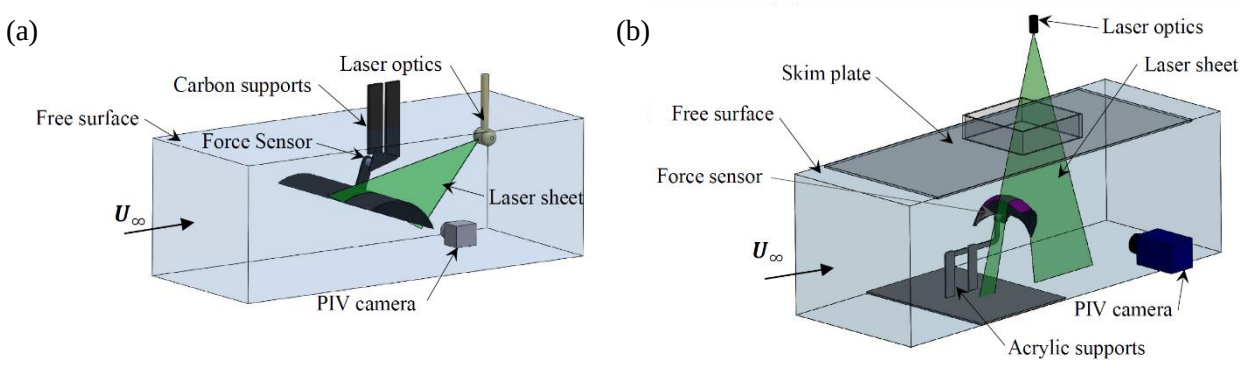

Figure 4: Experimental setup for (a) the circular arc and (b) the sail.

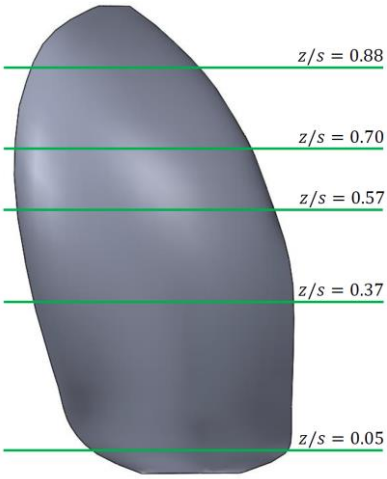

Figure 5: Spanwise location of the PIV planes for the three-dimensional sail.

2.3 FORCE MEASUREMENTS AND UNCERTAINTY

In both facilities, the lift L and drag D are recorded at 1000 Hz for a minimum of 6 s in the towing tank (limited by the run length) and 60 s in the water tunnel. The lift and drag coefficients C_L and C_D are given in Equation (4) and (5), respectively.

$$C_L = \frac{2L}{\rho A U_\infty^2} \tag{4}$$

and

$$C_D = \frac{2D}{\rho A U_\infty^2}, \tag{5}$$

where L and D are the time-averaged lift and drag force measurements, respectively; ρ is the water density in accordance with the ITTC (2011); A is the area, defined as the planform area $A = cs$ for the circular arc and the surface area for the sail; and U_∞ is the carriage speed in the towing tank, and the flow velocity in the water tunnel.

The uncertainty U of the force measurement is given as the root sum of precision P and the total bias B_T such that

$$U = \sqrt{P^2 + B_T^2}. \tag{6}$$

The precision P of each individual measurement ($n = 1$), given at the 95% confidence level, corresponding to two standard deviations 2σ, is

$$P = \frac{2\sigma}{\sqrt{n}}. \tag{7}$$

The total bias of the force coefficient $B_T(C_F)$, where C_F may either be the lift of drag coefficient, is computed as

$$B_T(C_F) = \sqrt{\left(\frac{\partial C_F}{\partial \rho} B(\rho)\right)^2 = \left(\frac{\partial C_F}{\partial A} B(A)\right)^2 = \left(\frac{\partial C_F}{\partial U_\infty} B(U_\infty)\right)^2 = \left(\frac{\partial C_F}{\partial F} B(F)\right)^2}, \tag{8}$$

where the bias limits are summarised in Table 3 for the circular arc and Table 4 for the sail.

Table 3: Summary of bias limits for the circular arcs.

Bias Limit	Towing Tank			Water Tunnel
	Small Arc	Medium Arc	Large Arc	Large Arc
$B(\rho)$ [kg m^{-3}]	0.0397	0.0397	0.0397	0.286
$B(A)$ [m^2]	1.916×10^{-4}	1.996×10^{-4}	2.103×10^{-4}	2.103×10^{-4}
$B(U_\infty)$ [m s^{-1}]	0.005	0.005	0.005	0.00246
$B(F)$ [N]	0.0005	0.0005	0.0005	0.00625
$B_T(C_L)$ [-]	0.013	0.016	0.018	0.017
$B_T(C_D)$ [-]	0.010	0.010	0.011	0.010

Table 4: Summary of bias limits for the sails.

Bias Limit	Small Sail	Medium Sail	Large Sail
$B(\rho)$ [kg m^{-3}]	0.0423	0.0424	0.0285
$B(A)$ [m^2]	6.234×10^{-5}	7.792×10^{-5}	9.350×10^{-4}
$B(U_\infty)$ [m s^{-1}]	0.00257	0.00206	0.00171
$B(F)$ [N]	0.00625	0.00625	0.00625
$B_T(C_L)$ [-]	0.055	0.052	0.048
$B_T(C_D)$ [-]	0.032	0.032	0.032

2.4 PARTICLE IMAGE VELOCIMETRY AND UNCERTAINTY

Particle image velocimetry measurements were performed parallel to the onset flow and orthogonal to the tested geometries on their suction side. Here, planar PIV (or two-dimensional PIV), is undertaken using a 200 mJ Nd:YAG pulsed laser at a 532 nm wavelength, illuminating silver-coated hollow glass spheres (14 μm diameter).

For the circular arc, the laser sheet was generated using underwater optics. The PIV images were recorded at 7.5 Hz using a 5 Megapixel CCD (charge-coupled device) camera. For the sail, the laser sheet was created using a sheet optic and shone vertically downwards. The PIV images were recorded at 15 Hz using a 5.5 Megapixel sCMOS (scientific complementary metal–oxide–semiconductor) camera. PIV images were processed using one initial 96 px by 96 px pass with 50% overlap, before three 32 px by 32 px passes with a 75% overlap. As such, a velocity vector is ascertained for an 8 px by 8 px window.

The error in the velocity measurements is considered to be driven by the error in pixel displacement for the PIV measurements $\varepsilon_{\mathrm{PIV}}$ (Corkery et al, 2018). This is quantified using the linear sum of the fixed bias error $\varepsilon_{\mathrm{bias}}$, the particle image diameter error $\varepsilon_{\mathrm{rms},\Phi}$, the particle image displacement error $\varepsilon_{\mathrm{rms},\delta}$, the interrogation window particle density error $\varepsilon_{\mathrm{rms},\rho}$, and the variations in particle image intensity $\varepsilon_{\mathrm{rms,i}}$. The linear sum of the uncertainty components yields the error in pixel displacement

$$\varepsilon_{\mathrm{PIV}} = \varepsilon_{\mathrm{bias}} + \varepsilon_{\mathrm{rms},\Phi} + \varepsilon_{\mathrm{rms},\delta} + \varepsilon_{\mathrm{rms},\rho} + \varepsilon_{\mathrm{rms,i}}. \quad (9)$$

The overall pixel displacement measurement uncertainty is 0.0768 px for the circular arc and 0.0672 px for the sail. The various components of the uncertainty are summarised in Table 5.

Table 5: Summary of the PIV uncertainty.

Geometry	$\varepsilon_{\mathrm{PIV}}$ [px]	$\varepsilon_{\mathrm{bias}}$ [px]	$\varepsilon_{\mathrm{rms},\Phi}$ [px]	$\varepsilon_{\mathrm{rms},\delta}$ [px]	$\varepsilon_{\mathrm{rms},\rho}$ [px]	$\varepsilon_{\mathrm{rms,i}}$ [px]
Circular arc	0.0768	0.0132	0.0009	0.0030	0.0019	0.0578
Sail	0.0672	0.0016	0.0033	0.0030	0.0020	0.0578

3. RESULTS

3.1 VALIDATION

Force measurements acquired in the towing tank are validated against the wind tunnel tests of Velychko (2014) for the lift and drag coefficients, as presented in Figure 6(a) and 6(b), respectively. Both experiments were conducted at $Re = 53\,530$ for a circular arc with $y_c/c = 0.2232$. However, Velychko's arc features a higher thickness-to chord-ratio, $t/c = 0.0357$, and a higher aspect ratio $AR = 10$ compared to the present experiments where $t/c = 0.0090$ and $AR = 1.85$.

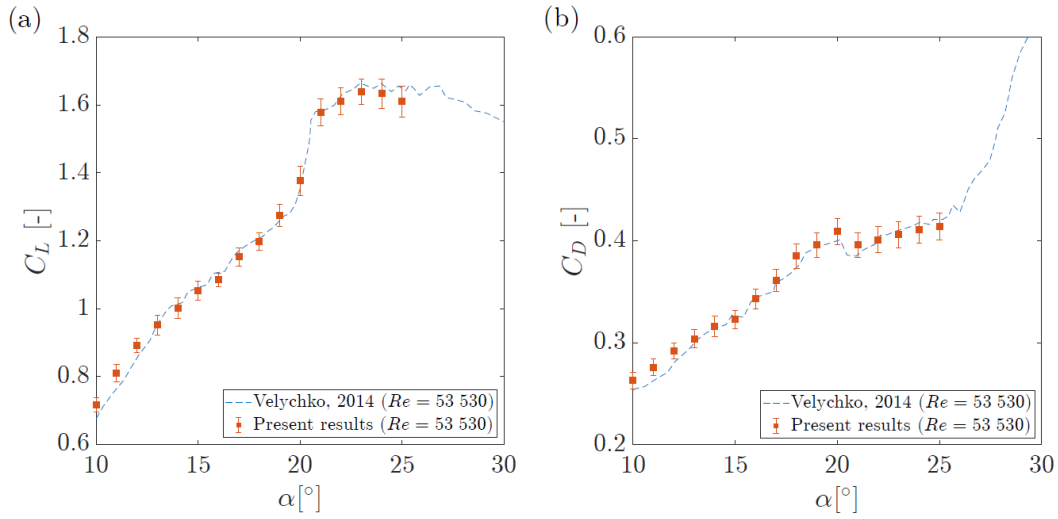

Figure 6: Measured lift (a) and drag (b) coefficient compared to Velychko (2014).

The agreement between the two sets of results demonstrates the validity of the proposed experimental methodology and the effectiveness of the end-plates in achieving an infinite aspect ratio. Moreover, because the thickness-to-chord ratios yield similar results, their effect is deemed negligible and thus applicable to infinitely thin arcs.

3.2 BLOCKAGE CORRECTION

The cross-section of experimental facilities constrains the flow around the tested geometry. Consequently, blockage corrections are routinely employed. However, because both the circular arc and sail feature a high camber, leading to a lift-generating body with a large region of trailing-edge separation, standard blockage corrections do not apply (Souppez & Viola, 2022). These include Pope and Harper (1966), ESDU 76028 (ESDU, 1995), ESDU 80024 (ESDU, 1998) and Barlow et al. (1999). Therefore, a dedicated blockage correction is devised experimentally for each geometry by repeating tests for increasing blockage ratios.

3.2 (a) 2D Circular Arc

For the circular arc, the blockage ratio is varied by means of the adjustable side walls presented in Section 2.1, yielding blockage ratios up to $A_F/A_S = 0.2477$. Experiments were conducted at $\alpha = 5°$, 10°, 15° and 20°. When no side walls are used, the lift and drag coefficients C_L and C_D are considered free-flow coefficients, i.e. not affected by blockage effects. When side walls are present, the coefficients with blockage are defined as C_{LB} and C_{DB} for the lift and drag, respectively. Thus, as the blockage ratio tends towards 0, C_L/C_{LB} and C_D/C_{DB} tend toward 1. This is depicted for the lift and drag in Figure 7(a) and (b).

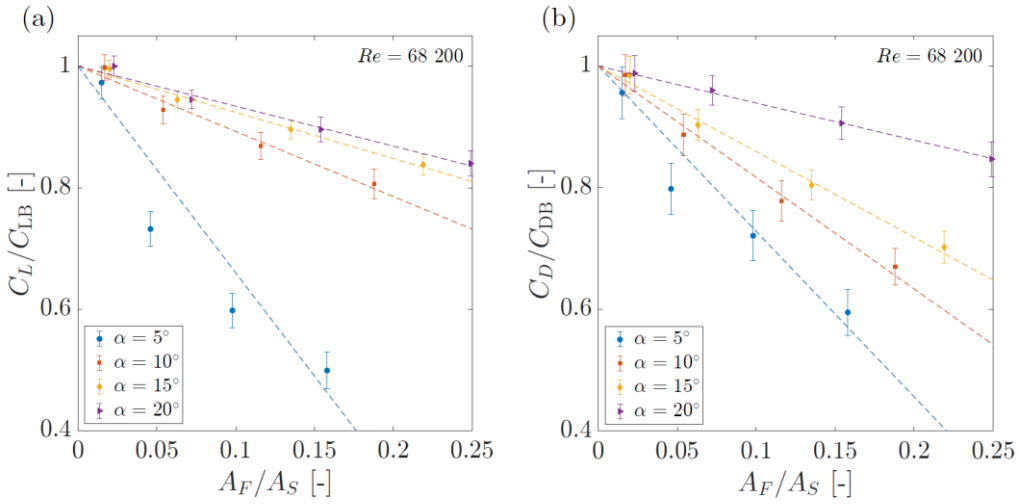

Figure 7: Effect of blockage ratio on (a) the lift and (b) the drag coefficient of the circular arc.

A linear trend is evidenced for $\alpha = 10°$, $15°$ and $20°$. This is not the case for $\alpha = 5°$, as the incidence is well below the ideal angle of attack (Souppez et al., 2022). This has been shown by Bot (2020) to result in a large recirculation bubble on the pressure side of the arc. Despite the high blockage ratios encountered, a linear blockage correction can be experimentally ascertained, thereby overcoming the limitations associated with high spatial resolution in two-dimensional sections, as later demonstrated in Section 3.3(a), where force measurements can be accurately corrected for blockage effects.

3.2 (b) 3D Sail

For the three-dimensional sail, the blockage ratio is now varied by employing various model-scale geometries, previously introduced in Section 2.2. Because the water tunnel does not enable to obtain free-flow coefficients, the results in Figure 8 present the evolution of the force coefficients with blockage effects, C_{LB} and C_{DB}. These are consistent with the expected effect of blockage, namely an increase in lift and drag coefficients for increasing blockage ratios.

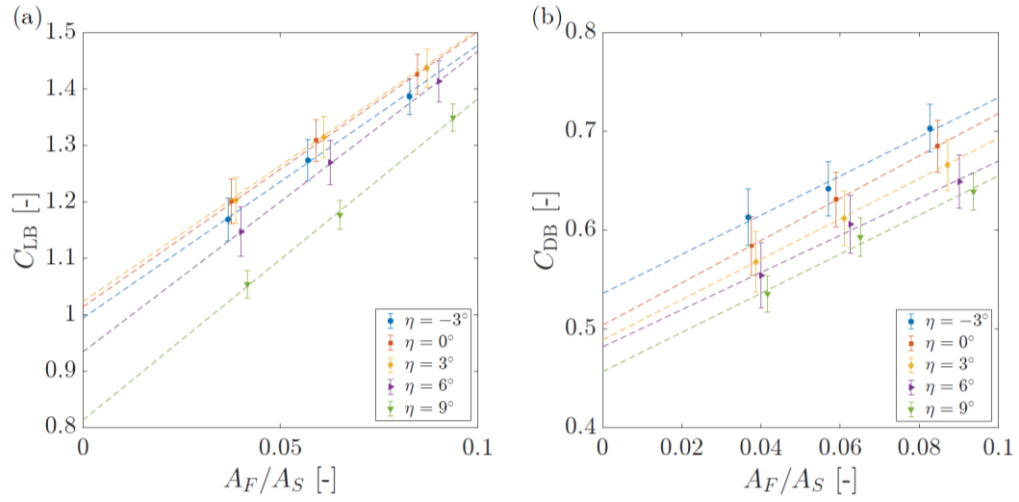

Figure 8: Effect of blockage ratio on (a) the lift and (b) the drag coefficient of the sail.

In three dimensions, for a range of rotation angles $-3° \leq \eta \leq 9°$, where $\eta = 0°$ is the intended operating angle for the sail, linear trends are also evidenced. This is significant because it allows extrapolation of the free-flow coefficients, the values of which are consistent with that of the offshore racing congress (ORC, 2023), as later evidence in Section 3.3(b). This section has demonstrated that the high blockage ratios arising from a high spatial resolution can be overcome, and force coefficients can accurately be corrected for the complex geometries under study, as shown in Section 3.3.

3.3 FORCE CRISIS

3.3 (a) 2D Circular Arc

A force crisis, characterised by a step increase in the trend of the lift coefficient with α, and a step decrease in the drag coefficient with α is visible in Figure 9(a) for C_L and Figure 9(b) for C_D. The force crisis is further identified by looking at the lift-to-drag ratio in Figure 9(c) and the lift versus drag coefficient in Figure 9(d). No force crisis is visible at $Re = 218\,000$ because it would occur for $\alpha < 5°$. Indeed, as shown by Bot et al. (2016), the force crisis for $Re = 200\,000$ occurs at $\alpha = 0°$. The results in Figure 9 also include the corrected force coefficients using the linear blockage correction devised in Section 3.2, demonstrating a very strong agreement with free-flow coefficients.

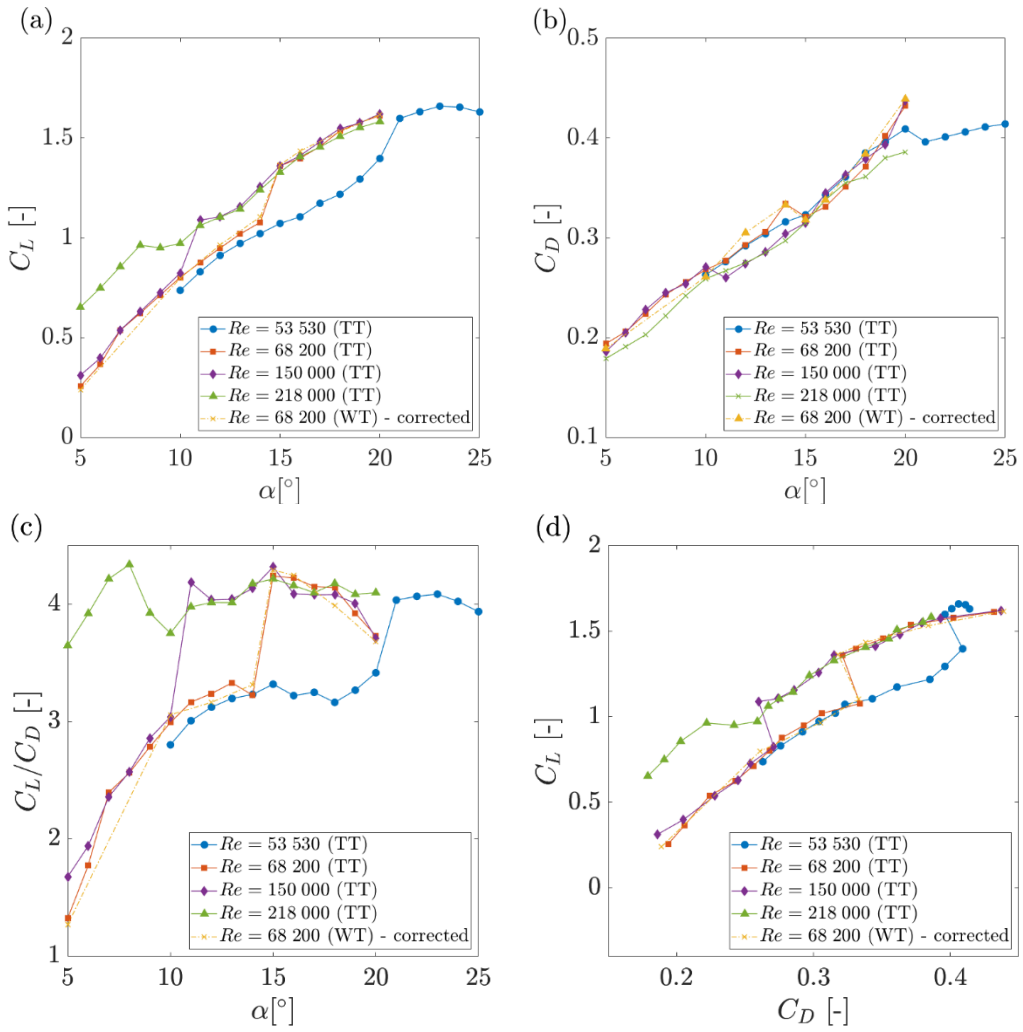

Figure 9: (a) Lift coefficient, (b) drag coefficient, (c) lift/drag ratio versus angle of attack, and (d) lift versus drag coefficient for $53\,530 \leq Re \leq 218\,000$.

Figure 9 presents a force crisis occurring at a given Re and triggered by a specific angle of attack, termed critical angle of attack α_{crit}. However, a force crisis can also occur for a fixed α once a specific Re is reached; this is known as a critical Reynolds number, Re_{crit}. Both behaviours are presented in Figure 10. In Figure 10(a), the circular arc at $\alpha = 11°$ evidences a critical Reynolds number such that $142\,000 \leq Re_{\text{crit}} \leq 146\,000$. Conversely, in Figure 10(b), the circular arc operates at $Re = 150\,000$, for which the critical angle of attack is $10° \leq \alpha_{\text{crit}} \leq 11°$.

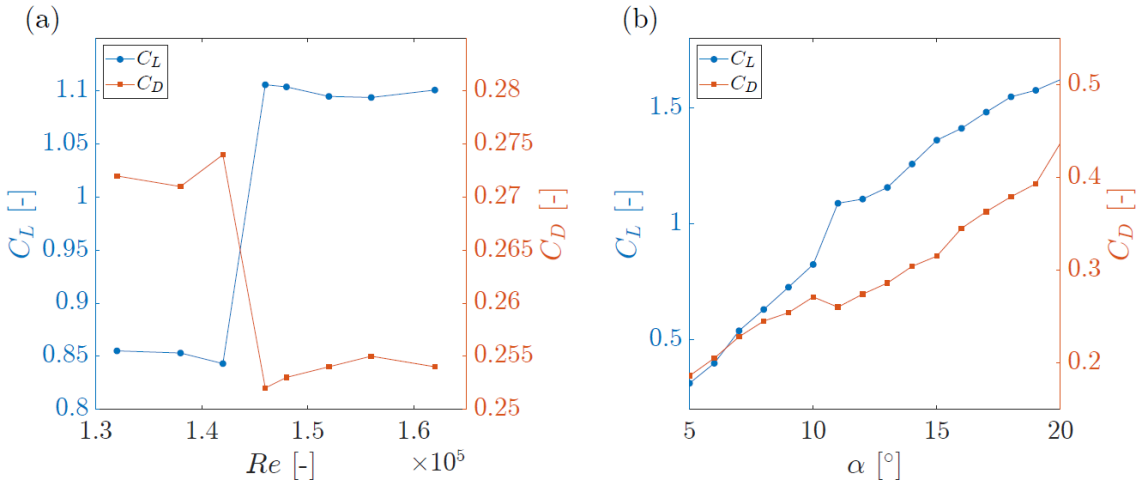

Figure 10: Lift and drag coefficient (a) versus Re for $\alpha = 11°$, and (b) versus α for $Re = 150\,000$.

When $Re < Re_{\text{crit}}$ and $\alpha < \alpha_{\text{crit}}$, the arc operates in subcritical regime, and laminar separation is expected. When either $Re > Re_{\text{crit}}$ or $\alpha > \alpha_{\text{crit}}$, then the arc operates in transcritical regime, where transition is expected to occur in the boundary layer and lead to turbulent separation, as on circular cylinders (Bloor, 1964; Zdravkovich, 1997). However, while the force measurements may suggest the same flow physics as on circular cylinders applies to circular arcs, the flow visualisation in Section 3.4 will demonstrate this is not always the case. This provides further emphasis on the need to achieve quantitative flow visualisations with PIV in addition to force measurements.

The present results complete the existing literature (Velychko,2014; Bot et al., 2016; Bot, 2020) and reveal that there exists a linear relationship between Re and α to yield either a subcritical or transcritical flow regime. This is significant as it enables model-scale experiments to be conducted in transcritical regime, which is representative of full-scale, and thus achieve suitable results. As such, the present work informs the design of model-scale experiments at low Re.

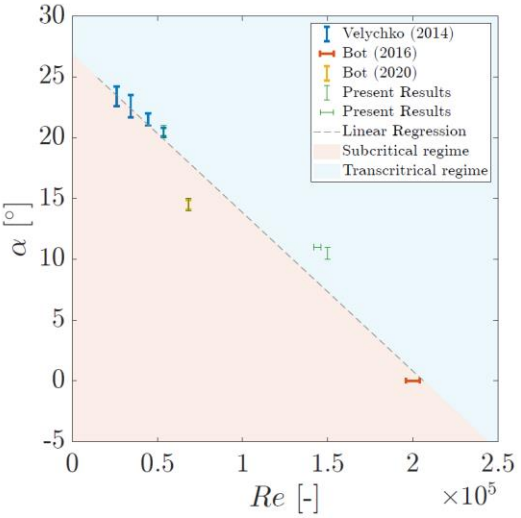

Figure 11: Reynolds number versus angle of attack and associated flow regimes.

3.3 (b) 3D Sail

For the three-dimensional sail, a force crisis is also evidenced in Figure 12, and shown to occur at the same $Re_{\bar{c}}$ for all blockage ratios. Thus, the force crisis is shown to be independent of the blockage ratio. Both the extrapolated lift and drag coefficients, presented in Figure 12(a) and 12(b), respectively, show a strong agreement with the expected coefficients (ORC, 2023). Blockage effects can, therefore,

also be accounted for in three dimensions. It is noted that, in Figure 12(b), the force crisis in 3D yields a step increase in the drag coefficient, as opposed to a step decrease for the 2D geometry. This is due to the induced drag component, proportional to C_L^2, which occurs only in 3D.

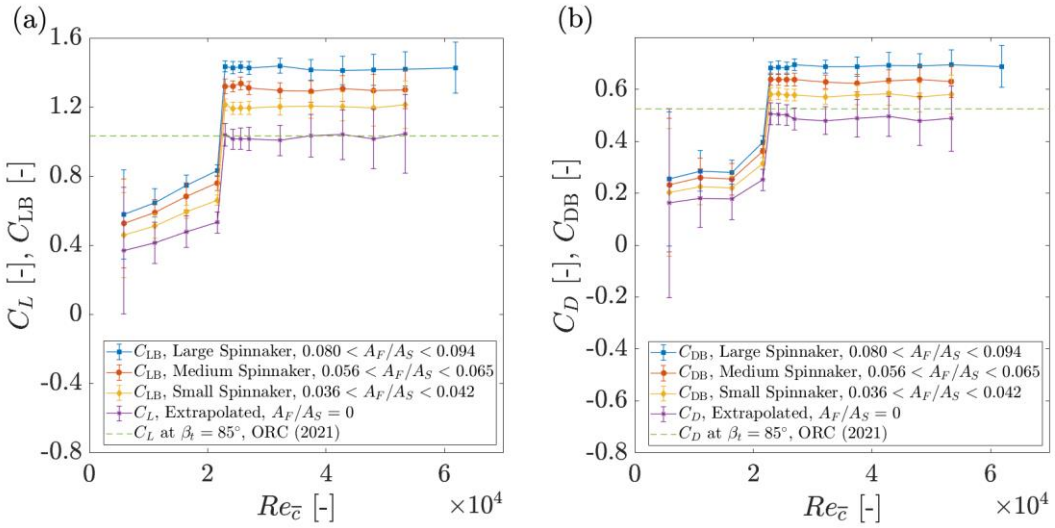

Figure 12: Critical Reynolds number for the lift (a) and drag (b) coefficient at $\eta = 0°$.

In Figure 12, the force crisis is presented for a fixed rotation angle $\eta = 0°$ versus varying $Re_{\bar{c}}$. In Figure 13, a force crisis is also evidenced for a fixed $Re_{\bar{c}} = 22\,940$ versus varying η. The force crisis is not visible at $Re_{\bar{c}} = 32\,210$ because, as shown in Figure 12, the critical Reynolds number has been exceeded.

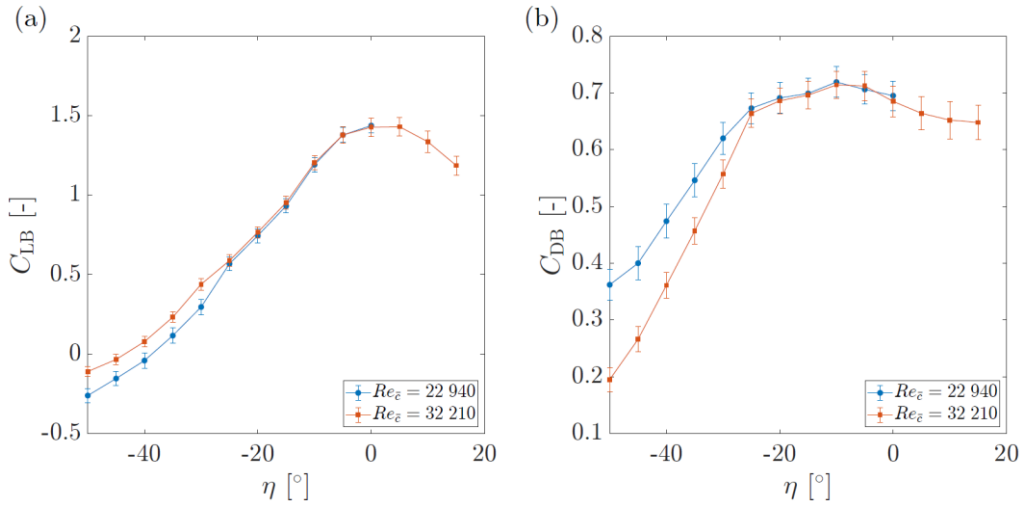

Figure 13: Critical η of the large spinnaker for (a) the lift coefficient, (b) the drag coefficients.

In this section, the accuracy of the blockage correction has been evidenced, together with the occurrence of a blockage-independent critical Reynolds number and critical angle of attack. These parameters are crucial to ensure flow conditions representative of full-scale are achieved. However, the underpinning flow physics is not as may be expected on circular cylinders (Bloor, 1964; Zdravkovich, 1997).

3.4 FLOW VISUALISATION

3.4 (a) 2D Circular Arc

The flow around the circular arc has been described by Bot (2020), and for α >11°, a LESB is expected. The laminar or turbulent nature of the flow, however, remains to be characterised. This is assessed using the turbulent kinetic energy κ, such that

$$\kappa = \frac{\overline{(u')^2} + \overline{(v')^2} + \overline{(w')^2}}{2}, \tag{10}$$

where the variance in flow velocity in the streamwise, streamnormal and crossflow directions are labelled $\overline{(u')^2}$, $\overline{(v')^2}$ and $\overline{(w')^2}$, respectively. Given the planar PIV setup used (see Section 2.2) and the absence of an out-of-plane component, $\overline{(w')^2}$ is neglected. Here, the flow is considered turbulent for $\kappa > 0.01U_\infty^2$, which has proven applicable to a range of geometries and flow conditions (Crompton and Barrett, 2000; Langari and Yang, 2013; Sampaio et al., 2014; Lee et al., 2015; Breuer, 2018). In Figure 14(a) at $\alpha = 13°$, i.e. subcritical regime, the laminar separation is visible, with turbulent kinetic energy only present in the wake, downstream of the trailing edge-separation point represented by a red diamond. Conversely, in Figure 14(b) at $\alpha = 16°$, i.e. transcritical regime, turbulent kinetic energy is visible upstream of the point of trailing edge separation. However, at this scale, the flow in the LESB and boundary layer is not clearly visible, hence the zoomed-in views of the leading edge at $\alpha = 13°$ and $\alpha = 16°$ in Figure 14(c) and 14(d), respectively. The former shows a turbulent LESB, followed by a laminar boundary layer, suggesting relaminarisation occurs in subcritical regime. Conversely, a turbulent boundary layer follows a turbulent LESB in transcritical regime.

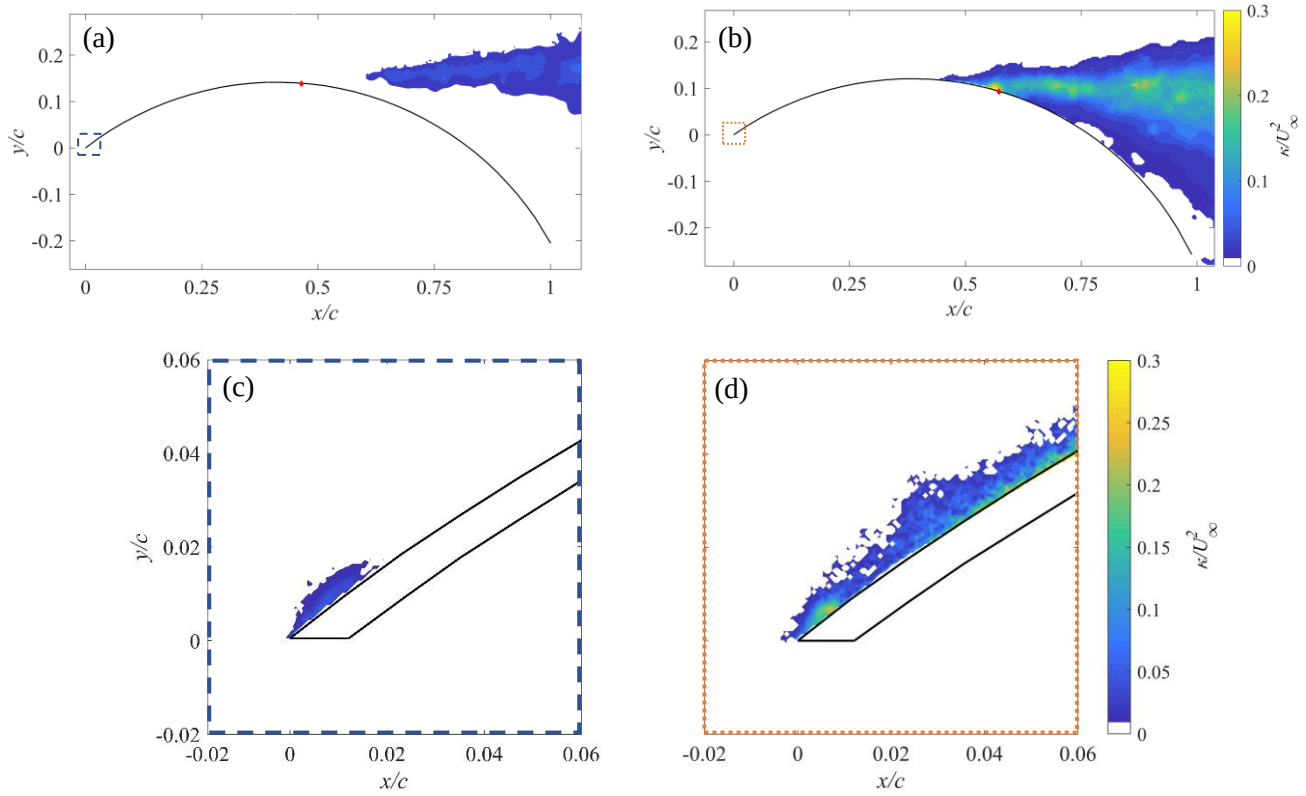

Figure 14: Non-dimensional turbulent kinetic energy for the whole arc at (a) $\alpha = 13°$ and (b) $\alpha = 16°$, at and leading edge at (c) $\alpha = 13°$ and (d) $\alpha = 16°$, for $Re = 68\,200$.

Relaminarisation can occur for high streamwise velocity gradients du/dx, expected on highly cambered geometries. The PIV findings using κ were confirmed by applying the relaminarisation

criterion of Narasimha and Sreenivasan (1979), based on the acceleration parameter K of Launder (1992), such that

$$K = \frac{\nu}{u^2}\frac{du}{dx} \geq 3.5 \times 10^{-6}, \tag{11}$$

where ν is the kinematic viscosity, and u is the streamwise flow velocity. Therefore, the force crisis on the circular arc originates from the suppressed relaminarisation of the boundary layer downstream of a turbulent LESB and not transition in the boundary layer as on circular cylinders. Whether these findings remain valid in three dimensions will be ascertained on the 3D sail.

3.4 (b) 3D Sail

First, the flow fields around the 3D sail under consideration are characterised at $z/s = 0.05$, 0.37, 0.57, 0.70 and 0.88 in both subcritical ($Re_{\bar{c}} = 16\,320$) and transcritical ($Re_{\bar{c}} = 32\,210$) regime to identify where a LESB might occur. Figure 15 presents the streamlines and resultant velocity $|V|$, defined as

$$|V| = \sqrt{u^2 + v^2}, \tag{12}$$

where v is the streamnormal flow velocity. A LESB is visible at $z/s = 0.37$ for both $Re_{\bar{c}}$ and identifiable in Figure 15(g) and 15(h).

The laminar or turbulent nature of the flow is then presented in Figure 16, using the previously employed $\kappa > 0.01U_\infty^2$ threshold for turbulent flow. Transcritical regime ($Re_{\bar{c}} = 32\,210$) reveals turbulent trailing-edge separation at all investigated spanwise section, which is not the case in subcritical regime ($Re_{\bar{c}} = 16\,320$). At $z/s \geq 0.57$, the results are similar to that of circular cylinders (Bloor, 1964; Zdravkovich, 1997). Remarkably, at $z/s = 0.37$, the only spanwise section where a LESB occurs, both LESBs are clearly turbulent, as shown in Figure 16(g) and 16(h). However, in subcritical regime (Figure 16(g)), the former relaminarizes before transition in the downstream boundary layer. Conversely, in transcritical regime (Figure 16(h)) relaminarisation does not occur. These findings are consistent with the behaviour of the 2D circular arc presented in Section 3.4(a). Finally, at $z/s = 0.05$, turbulent trailing-edge separation occurs at both $Re_{\bar{c}}$. This is understood as the effect of the large tip vortex occurring at the bottom of the sail (Viola et al., 2014) and thus would be expected to occur at any $Re_{\bar{c}}$.

In this section, the flow physics underpinning the force crisis has been characterised. For both the 2D circular arc and 3D sail, the LESB has been shown to always be turbulent. In subcritical regime, the spanwise velocity gradient arising from the highly cambered geometry is sufficient to cause relaminarisation of the boundary layer downstream of the LESB. Consequently, the force crisis is associated with the suppressed relaminarisation of the boundary layer downstream of the LESB. This is of particular relevance to the model testing of wind-assisted ship and yacht sails: these thin wings will experience the formation of a LESB for incidences between the ideal angle of attack (minimum required to inflate a soft sail without inflexion) and stall. Therefore, model-scale experiments must ensure either the critical angle of attack or critical Reynolds number is exceeded so that relaminarisation downstream of the LESB is suppressed. These values cannot be ascertained at priori, and thus the present work also offers a relevant methodology for the experimental testing of wings and sails for wind-assisted ships and yachts.

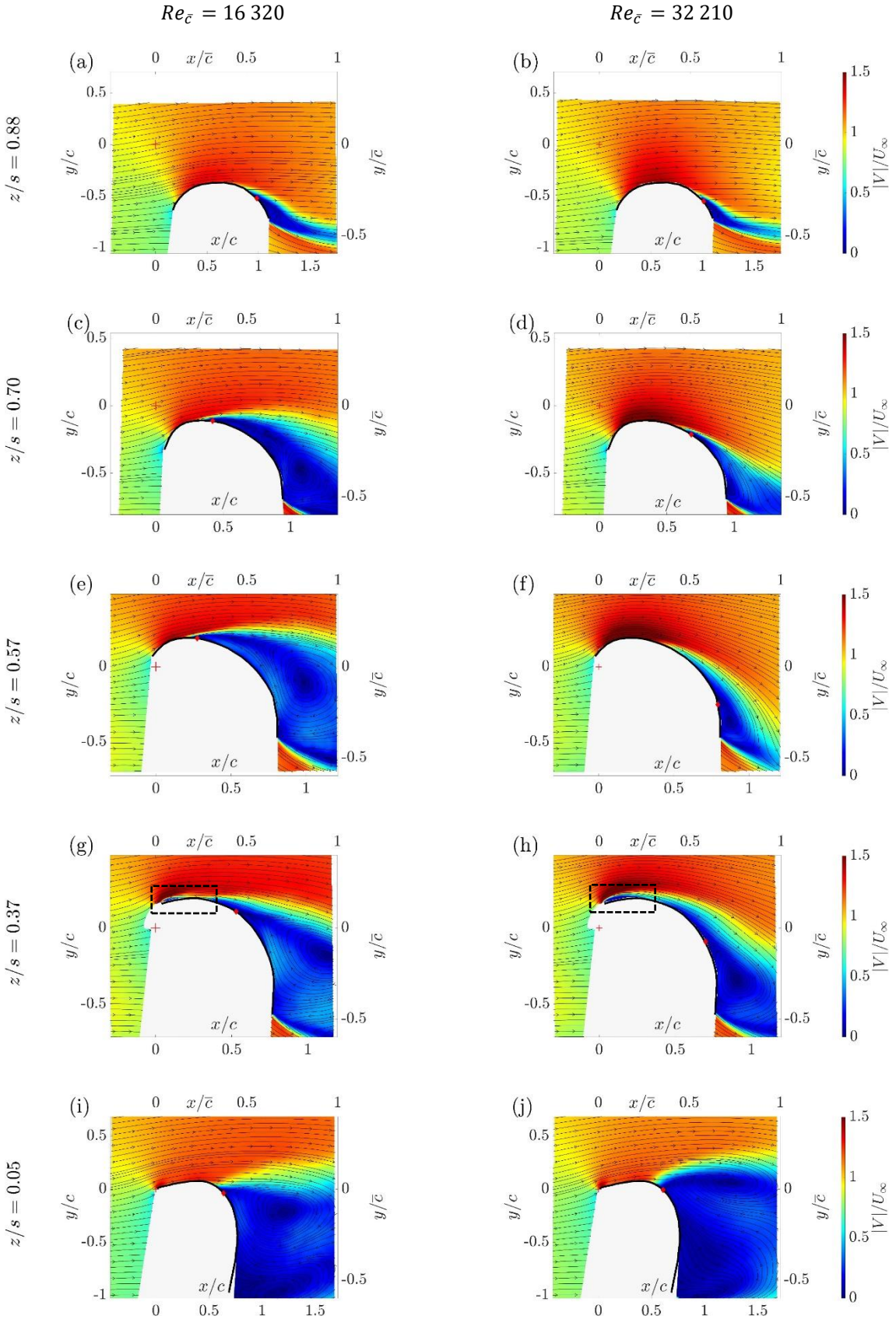

Figure 15: Non-dimensional resultant velocity and streamlines for the large sail at $Re_{\bar{c}} = 16\,320$ and $Re_{\bar{c}} = 32\,210$.

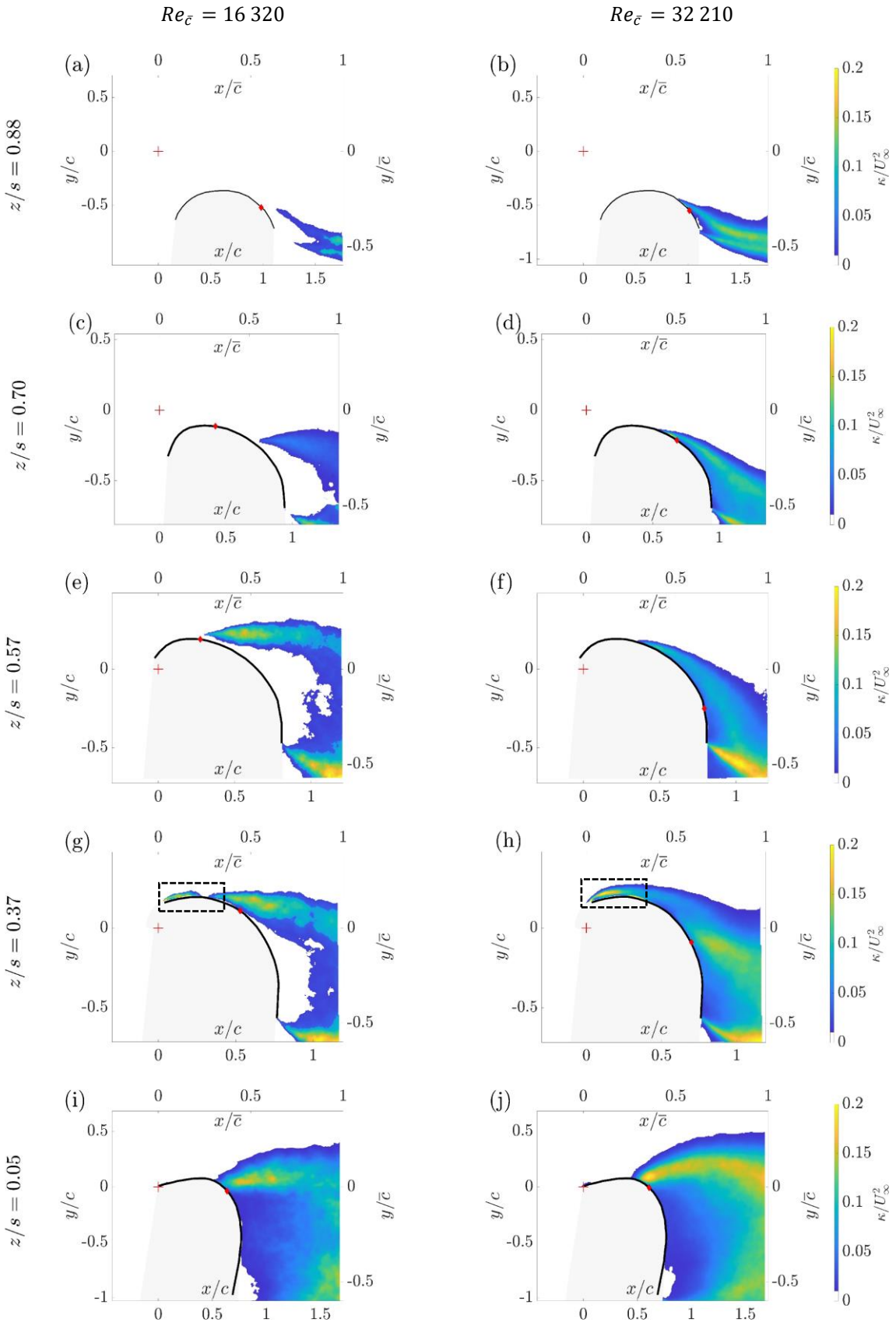

Figure 16: Non-dimensional turbulent kinetic energy for the large sail at $Re_{\bar{c}} = 16\,320$ and $Re_{\bar{c}} = 32\,210$.

4. CONCLUSIONS

The paper addressed the emerging practice of undertaking aerodynamic experiments in water tunnels to facilitate particle image velocimetry flow measurements. Two geometries were investigated, a two-dimensional circular arc and a three-dimensional sail, both relevant to wind-assisted ships and yachts. The aim was to ascertain whether experiments conducted at a high blockage ratio and a low Reynolds number could provide the required high spatial and temporal resolution without affecting the accuracy of the results.

For both geometries, the high blockage ratios can be accounted for with a linear blockage correction devised experimentally. Furthermore, there exists and blockage-independent critical Reynolds number and critical angle of attack. These yield a force crisis necessary for force coefficients to match that of full-scale wings and sails. Force measurement alone might have suggested the force crisis resulted from the laminar-to-turbulent transition of the boundary layer. However, the quantitative flow measurements undertaken revealed that the force crisis results from the suppressed relaminarisation of the boundary layer downstream of a leading-edge separation bubble.

These results provide new insights that not only demonstrate the relevance of the proposed experimental approach but its necessity to achieve new aerodynamic breakthroughs for wind-assisted ships and racing yachts alike. It is envisaged these findings will support the refinement of experimental testing procedures to maximise spatial and temporal resolution, thereby ensuring accurate and reproducible results and ultimately leading to better performance by design.

5. REFERENCES

Arredondo Galeana, A., (2019), A study of the vortex flows of downwind sails, PhD Thesis, The University of Edinburgh.

Arredondo-Galeana, A., and Viola, I.M., (2018), The leading-edge vortex of yacht sails, Ocean Engineering, 159, 552–562.

Arredondo-Galeana, A., Babinsky, H., and Viola, I.M., (2023), Vortex flow of downwind sails. Flow, 3: E8.

Atkinson, G.M. and Binns, J., (2018), Power profile for segment rigid sail, Journal of Marine Engineering & Technology, 17(2): 99-105.

Bloor, S., (1964), The transition to turbulence in the wake of a circular cylinder, Journal of Fluid Mechanics, 19(2): 290–304.

Bordogna, G., (2020), Aerodynamics of wind-assisted ships: interaction effects on the aerodynamic performance of multiple wind-propulsion systems, PhD Thesis, TU Delft.

Bordogna, G., Keuning, J.A., Huijsmans, R.H.M. and Belloli, M., (2018), Wind-tunnel experiments on the aerodynamic interaction between two rigid sails used for wind-assisted propulsion, International Shipbuilding Progress, 65(1): 93-125.

Bordogna, G., Muggiasca, S., Giappino, S., Belloli, M., Keuning, J.A. and Huijsmans, R.H.M., (2020), The effects of the aerodynamic interaction on the performance of two Flettner rotors, Journal of Wind Engineering and Industrial Aerodynamics, 196: 104024.

Bot, P., (2020), Force variations related to flow pattern changes around a high-camber thin wing, AIAA Journal, 58(5): 1906–1912.

Bot, P., Rabaud, M., Thomas, G., Lombardi, A., and Lebret, C., (2016), Sharp transition in the lift force of a fluid flowing past nonsymmetrical obstacles: evidence for a lift crisis in the drag crisis regime, Physical review letters, 117(23): 234501.

Bot, P., Viola, I.M., Flay, R.G.J., and Brett, J.-S., (2014), Wind-tunnel pressure measurements on model scale rigid downwind sails. Ocean Engineering, 90: 84–92.

Braun, J., Richelsen, M., Schreber, M., (2016), Downind aero moments & forces - phase 2C, Sailing Yacht Research Foundation, Warwick, Rhode Island, USA.

Campbell, I.M.C., (2014), A comparison of downwind sail coefficients from tests in different wind tunnels, Ocean Engineering, 90: 62-71.

Collie S., (2006), Application of computational fluid dynamics of two dimensional downwind sail flows, PhD thesis, Faculty of Mechanical Engineering, University of Auckland.

Deparday, J., Augier, B., and Bot, P., (2018), Experimental analysis of a strong fluid–structure interaction on a soft membrane - application to the flapping of a yacht downwind sail, Journal of Fluids and Structures, 81: 547–564.

Dewavrin, J. and Souppez, J.-B.R.G., (2018), Experimental investigation into modern hydrofoil-assisted monohulls: how hydrodynamically efficient are they?. Transactions of the Royal Institution of Naval Architects Part B: International Journal of Small Craft Technology, IJSCT223.

Fossati, F., Muggiasca, S., Viola, I.M. and Zasso, A., (2006), Wind tunnel techniques for investigation and optimization of sailing yachts aerodynamics, 2nd High Performance Yacht Design Conference, Auckland, New Zealand.

Gauvin, E., and Banks, J., (2020), Measuring the flow-field around flexible downwind sails using particle image velocimetry: A feasibility study into a new experimental approach for the investigation of sailing yacht aerodynamics, 5th International Conference on Innovation in High Performance Sailing Yachts and Sail-Assisted Ship Propulsion, 27–36.

Giovannetti, L.M., Dhome, U., Malmek, K., Persson, A. and Wielgosz, C., (2022), Multi-wing sails interaction effects, SNAME Chesapeake Sailing Yacht Symposium, Annapolis, Maryland, USA.

He, J., Hu, Y., Tang, J. and Xue, S., (2015), Research on sail aerodynamics performance and sail-assisted ship stability, Journal of Wind Engineering and Industrial Aerodynamics, 146: 81-89.

ITTC, (2011), ITTC recommended procedures - fresh water and seawater properties, International Towing Tank Conference, Rio de Janeiro, Brasil.

Khan, L., Macklin, J., Peck, B., Morton, O. and Souppez, J.-B.R.G., (2021), A review of wind-assisted ship propulsion for sustainable commercial shipping: latest developments and future stakes, Wind Propulsion Conference, Royal Institution of Naval Architects.

Kume, K., Hamada, T., Kobayashi, H. and Yamanaka, S., (2022), Evaluation of aerodynamic characteristics of a ship with Flettner rotors by wind tunnel tests and RANS-based CFD, Ocean Engineering, 254: 111345.

Lasher, W. C., Sonnenmeier, J. R., Forsman, D. R., and Tomcho, J., (2005), The aerodynamics of symmetric spinnakers, Journal of wind engineering and industrial aerodynamics, 93(4): 311–337.

Launder, B. E., (1992), Laminarisation of three-dimensional accelerating boundary layers in a curved rectangular-sectioned duct, International Journal of Heat and Fluid Flow, 13: 124–131.

Molina, A., De Troyer, T., Massai, T., Vergaerde, A., Runacres, M. C., and Bartoli, G., (2019), Effect of turbulence on the performance of vawts: An experimental study in two different wind tunnels, Journal of Wind Engineering and Industrial Aerodynamics, 193, 103969.

Narasimha, R. and Sreenivasan, K. R., (1979), Relaminarisation of fluid flows, Advances in Applied Mechanics, 19: 221–309 (1979).

ORC, (2023), ORC VPP Documentation, Offshore racing Congress.

Raffel, M., Willert, C.E., Scarano, F., Kähler, C.J., Wereley, S.T. and Kompenhans, J., (2018), Particle image velocimetry: a practical guide, Springer, ISBN : 978-3-319-68851-0.

Souppez, J.-B.R.G. and Viola, I.M., (2021), Circular arc aerodynamics and applications to downwind yacht sails and wind assisted ships, IX International Conference on Computational Methods in Marine Engineering.

Souppez, J.-B.R.G. and Viola, I.M., (2022), High-blockage corrections for circular arcs at transitional Reynolds numbers, Journal of Wind Engineering and Industrial Aerodynamics, 229: 105139.

Souppez, J.-B.R.G., Arredondo-Galeana, A. and Viola, I.M., (2019), Recent advances in numerical and experimental downwind sail aerodynamics, Journal of Sailing Technology, 4(01): 45-65.

Souppez, J.-B.R.G., Bot, P. and Viola, I.M. (2022), Turbulent flow around circular arcs, Physics of Fluids, 34(1): 015121.

Velychko, N., (2014), Study of highly cambered aerofoil using JR3 sensor, Department of Mechanical Engineering, The University of Auckland.

Viola, I.M. and Flay, R.G.J., (2009), Force and pressure investigation of modern asymmetric spinnakers. Transactions of the Royal Institution of Naval Architects Part B: International Journal of Small Craft Technology, 151(2), pp.31-40.

Viola, I.M., and Flay, R.G.J., (2010), Full-scale pressure measurements on a Sparkman and Stephens 24-foot sailing yacht, Journal of Wind Engineering and Industrial Aerodynamics, 98(12): 800–807.

Viola, I.M., Bartesaghi, S., Van-Renterghem, T., and Ponzini, R., (2014), Detached eddy simulation of a sailing yacht,Ocean Engineering, 90: 93–103.

Viola, I.M., Bot, P. and Riotte, M., (2013), Upwind sail aerodynamics: A RANS numerical investigation validated with wind tunnel pressure measurements, International Journal of Heat and Fluid Flow, 39: 90-101.

Zdravkovich, M. M., (1997), Flow Around Circular Cylinders: Fundamentals, Oxford Science Publications, ISBN-10 0198563965.

Zeng, Q., Zhang, X., Cai, W. and Zhou, Y., (2023), Wake distortion analysis of a Dynarig and its application in a sail array design, Ocean Engineering, 278: 114341.

Zhang, H., Hu, Y. and He, J., (2021), Wind tunnel experiment of multi-mode arc sail device, Polish Maritime Research, 28(4): 20-29.

Zhu, H., Nikmanesh, M.B., Yao, H.D., Ramne, B. and Ringsberg, J.W., (2022), Propulsive performance of a novel crescent-shaped wind sail analyzed with unsteady RANS, International Conference on Offshore Mechanics and Arctic Engineering, 85925: V007T08A053.